3D Shape Analysis for Early Diagnosis of Malignant Lung Nodules

Ayman El-Baz[1,⋆], Matthew Nitzken[1], Fahmi Khalifa[1], Ahmed Elnakib[1], Georgy Gimel'farb[2], Robert Falk[3], and Mohammed Abo El-Ghar[4]

[1] Bioimaging Laboratory, Bioengineering Department, University of Louisville, Louisville, KY, USA
Tel.: (502)-852-5092
aselba01@louisville.edu
[2] Department of Computer Science, University of Auckland, Auckland, New Zealand
[3] Department of Radiology, Jewish Hospital, Louisville, KY, USA
[4] Urology and Nephrology Department, University of Mansoura, Mansoura, Egypt

Abstract. An alternative method for diagnosing malignant lung nodules by their shape rather than conventional growth rate is proposed. The 3D surfaces of the detected lung nodules are delineated by spherical harmonic analysis, which represents a 3D surface of the lung nodule supported by the unit sphere with a linear combination of special basis functions, called spherical harmonics (SHs). The proposed 3D shape analysis is carried out in five steps: (*i*) 3D lung nodule segmentation with a deformable 3D boundary controlled by two probabilistic visual appearance models (the learned prior and the estimated current appearance one); (*ii*) 3D Delaunay triangulation to construct a 3D mesh model of the segmented lung nodule surface; (*iii*) mapping this model to the unit sphere; (*iv*) computing the SHs for the surface, and (*v*) determining the number of the SHs to delineate the lung nodule. We describe the lung nodule shape complexity with a new shape index, the estimated number of the SHs, and use it for the K-nearest classification to distinguish malignant and benign lung nodules. Preliminary experiments on 327 lung nodules (153 malignant and 174 benign) resulted in the 93.6% correct classification (for the 95% confidence interval), showing that the proposed method is a promising supplement to current technologies for the early diagnosis of lung cancer.

Keywords: Shape, Spherical Harmonics, Lung, Diagnosis, Nodules.

1 Introduction

Pulmonary nodules are the most common manifestation of lung cancer and are the principal cause of cancer-related deaths [16]. Fast and accurate classification of the nodules is of major importance for medical computer-aided diagnostic systems (CAD). A nodule is an approximately spherical volume of higher-density

⋆ Corresponding author.

G. Székely and H.K. Hahn (Eds.): IPMI 2011, LNCS 6801, pp. 772–783, 2011.

tissue visible in an X-ray lung image. Large malignant nodules (generally defined as greater than 1 cm in diameter) are easily detected with any traditional imaging equipment and are then diagnosed by needle biopsy or bronchoscopy. However, diagnostic options for small malignant nodules are limited due to difficulties in accessing them, especially if they are located deep in the tissue or away from the large airways. Therefore, additional imaging and CAD techniques are needed. The popular direction of detecting small cancerous nodules is to analyze their growth rate over time. This paper introduces a new approach to characterize detected nodules based on their shape.

Related work: A great deal of work has been published regarding the usefulness of morphologic features for discriminating malignant from benign pulmonary nodules on computed tomography (CT) and to a lesser extent, chest radiographs. Several studies have shown a correlation between different nodule shape characteristics and underlying pathology. For example, Furuya et al. [7] analyzed the margin characteristics of 193 pulmonary nodules on high-resolution CT and subjectively classified them as one of several types, including round, lobulated, densely spiculated, ragged, and halo. They found a high level of malignancy among the lobulated (82%), spiculated (97%), ragged (93%), and halo nodules (100%), while 66% of the round nodules proved to be benign.

Automatically extracted features have also been shown to correlate with underlying malignancy. Kawata et al. [10] quantified the surface curvature and degree of surrounding radiating pattern in biopsy-proven benign and malignant nodules, and compared the resulting feature maps. Their results showed good separation of the feature maps between the two categories. Similarly, fractal analysis has been used to quantify the nodule margin characteristics of benign and malignant nodules. Kido et al. [12] used 2D and 3D fractal dimensions to analyze the lung-nodule interface in a series of 117 peripheral pulmonary nodules of various underlying pathology including benign hamartomas, tuberculomas, and pneumonias as well as malignant diagnoses including brochogenic carcinomas. They noted statistically significant differences between the 2D fractal dimensions of hamartomas and all other nodules, as well as differences between the 3D fractal dimensions pneumonias and tuberculomas and bronchogenic carcinomas. Although none of these studies directly assessed the accuracy of their methods in predicting a diagnosis, they support the notion that nodule shape can potentially be used by automated systems to distinguish benign from malignant nodules.

Several groups have designed CAD systems with the goal of predicting a diagnosis based on features extracted from CT or chest radiographs. In general, they share common schema, first extracting features from the images, then designing and using an automatic classifier to categorize nodules based on these features, and lastly evaluating the performance of the system with receiver operating characteristics (ROC) analysis. The CAD systems differ in the specific extracted features and the type of classifier used, with linear discriminant classifiers (LDC) and neural networks (NN) being the most common. Below, LDCs-based classifier systems will be discussed followed by NN-based classifier systems.

Kawata and colleagues [11] designed a CT-based CAD system that classified pulmonary nodules based on a combination of their curvature index and the relationship of the nodules to their surrounding features. Mori et al. [13] also designed a CAD system using a curvedness index in combination with dynamic contrast-enhanced CT in order to evaluate temporal change as a possible discriminating feature of benign and malignant nodules.

One of the early neural network based CAD systems was developed by Gurney and Swensen [8]. They compared two systems, one using a neural network based classifier and one using a Bayesian classifier. Both systems used a combination of subjectively evaluated clinical and radiological characteristics including border smoothness, spiculation and lobulation.

In summary, the aforementioned existing approaches show the following limitations:

- Most of them classify the lung nodules based on extracted 2D features (e.g., round, lobulated, ragged, and halo, etc.) and they did not take into account the 3D features of lung nodules.
- Most of them did not provide a quantitative measure that has the ability to describe the shape complexity of detected lung nodules.
- Most of the existing features (e.g., curvature, round, etc.) depend on the accuracy of the used nodule segmentation algorithm which make them are difficult for clinical practitioners to use.

This work aims to address these limitations in a way that will make evaluating small lung masses more consistent.

2 Methods

In this work, we propose a novel shape-based approach for the analysis of lung nodules variability between malignant and benign nodules (see Fig. 1). *In this paper we will focus on the steps from 2 to 5 and the first step is shown in detail in [4].*

2.1 Lung Nodules Segmentation

Accurate lung nodules segmentation from 3D LDCT images is a challenging problem because the intensities of the lung nodules and surrounding tissues (e.g., blood vessels, chest, etc.) are not clearly distinguishable. To overcome this problem, we follow our approach introduced in [6], which depends on using a conventional 3D parametric deformable boundary [9], but control its evolution with two probabilistic visual appearance models, namely, a learned lung nodule appearance prior and a current appearance model of the image to be segmented. The prior is a 3D Markov-Gibbs random field (MGRF) model of the lung nodules' intensities with translation- and rotation-invariant pairwise voxel interaction, **being learned analytically based on developing a new maximum likelihood estimator from thevtraining data**. The current appearance is modeled

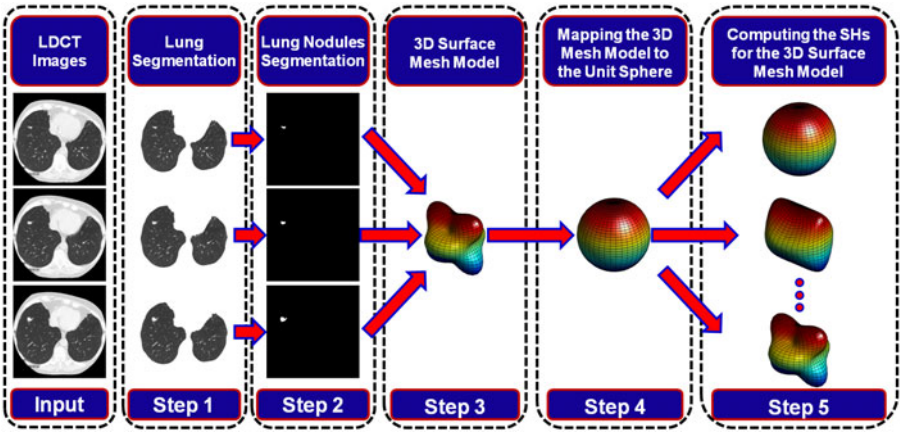

Fig. 1. Proposed shape-based system for early diagnosis of malignant nodules

by a mixed marginal distribution of the voxel intensities in both the lung nodule and surrounding tissues. To extract the voxel-wise model of the current nodule appearance, the mixture is precisely approximated with a linear combination of discrete Gaussians (LCDG) [3] and automatically separated into the lung nodule and background LCDG models. Let (x, y, z) be Cartesian 3D point coordinates. A conventional parametric deformable surface, $\mathbf{B}(\mathbf{P}_1, \ldots, \mathbf{P}_K)$, specified by K control vertices $\mathbf{P}_k = (x_k, y_k, z_k)$, evolves in the directions that minimize its energy, E, depending on internal, $\zeta_{\text{int}}(\mathbf{B})$, and external, $\zeta_{\text{ext}}(\mathbf{B})$, forces [9]:

$$E = E_{\text{int}} + E_{\text{ext}} \equiv \int_{\mathbf{B}} (\zeta_{\text{int}}(\mathbf{B}) + \zeta_{\text{ext}}(\mathbf{B}))\, d\mathbf{B} \tag{1}$$

In this paper, we introduce a new type of external energy that depends on both the learned prior and the current (on-going) appearance model. Let $\mathbf{Q} = \{0, 1, \ldots, Q-1\}$ and $\mathbf{L} = \{\mathsf{nl}, \mathsf{bg}\}$ be finite sets of image intensities (gray values) and region labels, respectively. Let a finite 3D arithmetic lattice $\mathbf{R} = [(x, y, z) : x = 0, \ldots, X-1; y = 0, \ldots, Y-1, z = 1, \ldots, Z-1]$ support a 3D image $\mathbf{g} : \mathbf{R} \to \mathbf{Q}$ and its region map $\mathbf{m} : \mathbf{R} \to \mathbf{L}$. The label, $m_{x,y,z}$, associates the voxel, $g_{x,y,z}$, with the lung nodule or the background. To reduce the impact of global contrast and offset deviations of intensities due to different sensors, each input 3D image is normalized by mapping its signal range $[q_{\min}, q_{\max}]$ to the maximal range of $[0, 255]$.

To consider the normalized images as samples of a prior MGRF model but exclude any image alignment before the segmentation, we use a generic translation- and rotation-invariant MGRF with only voxel-wise and central-symmetric pairwise voxel interaction. The latter is specified by a set $\mathbf{N}$ of characteristic central-symmetric voxel neighborhoods $\{\mathbf{n}_\nu : \nu \in \mathbf{N}\}$ on $\mathbf{R}$ and a corresponding set $\mathbf{V}$ of Gibbs potentials, one per neighborhood. A central-symmetric neighborhood $\mathbf{n}_\nu$ embraces all voxel pairs such that the (x, y, z)-coordinate offsets

between any voxel (x, y, z) and its neighbor (x', y', z') belong to an indexed semi-open interval $[d_{\nu,\min}, d_{\nu,\max})$; $\nu \in \mathbf{N} \subset \{1, 2, 3, \ldots\}$ of the inter-voxel distances: $d_{\nu,\min} \leq \sqrt{(x-x')^2 + (y-y')^2 + (z-z')^2} < d_{\nu,\max}$.

Learning the appearance prior. Let $\mathbf{S} = \{(g_t.m_t) : t = 1, \ldots, T\}$ be a training set of 3D images with known region maps. Let $\mathbf{R}_t = \{(x, y, z) : (x, y, z) \in \mathbf{R} \ \wedge \ m_{t;x,y,z} = \mathsf{nl}\}$ denote the part of $\mathbf{R}$ supporting lung nodule in the t-th training pair (g_t, m_t); $t = 1, \ldots, T$. Let $\mathbf{C}_{\nu,t}$ be a family of voxel pairs in $\mathbf{R}_t^2$ with the co-ordinate offset $(\xi, \eta, \gamma) \in \mathbf{n}_\nu$ in a particular neighborhood. Let $\mathbf{F}_{\mathrm{vx},t}$ and $\mathbf{F}_{\nu,t}$ be empirical marginal probability distributions of voxel intensities and of intensity co-occurrences, respectively, in the training lung nodule from $\mathbf{g}_t$: $\mathbf{F}_{\mathrm{vx},t} = \left[f_{\mathrm{vx},t}(q) = \frac{|\mathbf{R}_{t,q}|}{|\mathbf{R}_t|} : \ q \in \mathbf{Q}\right]$ and $\mathbf{F}_{\nu,t} = \left[f_{\nu,t}(q, q') = \frac{|\mathbf{C}_{\nu,t;q,q'}|}{|\mathbf{C}_{\nu,t}|} : \ (q, q') \in \mathbf{Q}^2\right]$ where $\mathbf{R}_{t,q} = \{(x, y, z) : (x, y, z) \in \mathbf{R}_t \wedge g_{x,y,z} = q\}$ is a subset of voxels supporting the intensity q and $\mathbf{C}_{\nu,t;q,q'}$ is a subset of the voxel pairs $\mathbf{c}_{\xi,\eta,\gamma}(x, y, z) = ((x, y, z), (x+\xi, y+\eta, z+\gamma)) \in \mathbf{R}_t^2$ supporting the intensity co-occurrence (q, q') in the training lung nodule from $\mathbf{g}_t$. Let $\mathbf{V}_{\mathrm{vx}} = [V_{\mathrm{vx}}(q) : q \in \mathbf{Q}]$ be a potential function of voxel intensities that describes the voxel-wise interaction. Let $\mathbf{V}_\nu = [V_\nu(q, q') : (q, q') \in \mathbf{Q}^2]$ be a potential function of intensity co-occurrences in the neighboring voxel pairs that describes the pairwise interaction in the neighborhood $\mathbf{n}_\nu$; $\nu \in \mathbf{N}$. The MGRF model of the t-th training pair is specified by the joint Gibbs probability distribution on the sublattice $\mathbf{R}_t$:

$$P_t = \frac{1}{Z_t} \exp\left(|\mathbf{R}_t| \left(\mathbf{V}_{\mathrm{vx}}^{\mathsf{T}} \mathbf{F}_{\mathrm{vx},t} + \textstyle\sum_{\nu \in \mathbf{N}} \rho_{\nu,t} \mathbf{V}_{\nu,t}^{\mathsf{T}} \mathbf{F}_{\nu,t}\right)\right) \tag{2}$$

where $\rho_{\nu,t} = |\mathbf{C}_{\nu,t}|/|\mathbf{R}_t|$ is the average cardinality of $\mathbf{n}_\nu$ with respect to $\mathbf{R}_t$.

To identify the MGRF model in Eq. (2), the Gibbs potentials are approximated analytically:

$$V_{\mathrm{vx},\mathsf{nl}}(q) = \log f_{\mathrm{vx},\mathsf{nl}}(q) - \frac{1}{Q} \sum_{\kappa \in \mathbf{Q}} \log f_{\mathrm{vx},\mathsf{nl}}(\kappa) \qquad \text{for } q \in \mathbf{Q}; \text{ and} \tag{3}$$

$$V_{\nu,\mathsf{nl}}(q, q') = \lambda \rho_\nu \left(f_{\nu,\mathsf{nl}}(q, q') - f_{\mathrm{vx},\mathsf{nl}}(q) f_{\mathrm{vx},\mathsf{nl}}(q')\right) \quad \text{for } (q, q') \in \mathbf{Q}^2 \tag{4}$$

where the common factor λ is also computed analytically.

Modeling the current appearance with LCDG. Non-linear intensity variations in a data acquisition system due to scanner type and scanning parameters affect visual appearance of lung nodules in each data set $\mathbf{g}$ to be segmented. Thus in addition to the learned appearance prior, an on-going lung nodule appearance within a current position of the evolving boundary $\mathbf{B}$ in $\mathbf{g}$ is modeled with its marginal intensity distribution. The whole marginal distribution of the voxel intensities within the boundary is considered as a dynamic mixture of two probability models that characterize the lung nodule and its background, respectively. The mixture is partitioned into these two LCDG models by using the EM-based approach detailed in [3].

Boundary evolution under the appearance models. Let $p_{\mathrm{vx},\mathsf{nl}}(q)$ be the marginal probability of the intensity q in the estimated current LCDG model

for the lung nodule. To guide the boundary evolution, we combine in the external energy term of Eq. (1), both the learned prior and the on-going nodule appearance model as follows:

$$\zeta_{\text{ext}}\left(\mathbf{P}=(x,y,z)\right) = -p_{\text{vx,nl}}(g_{x,y,z})\pi_{\mathbf{P}}(g_{x,y,z}|\mathbf{S}) \tag{5}$$

Here, $\pi_{\mathbf{P}}(q|\mathbf{S})$ is the prior conditional probability of q, given the fixed current intensities in the characteristic central-symmetric neighborhood of $\mathbf{P}$ for the MGRF prior model of Eq. (2):

$$\pi_{\mathbf{P}}(g_{x,y,z}|\mathbf{S}) = \exp(E_{\mathbf{P}}(g_{x,y,z}|\mathbf{S}))/\sum_{q\in\mathbf{Q}}\exp(E_{\mathbf{P}}(q|\mathbf{S}))$$

where $E_{\mathbf{P}}(q|\mathbf{S})$ is the conditional Gibbs energy of pairwise interaction for the voxel $\mathbf{P}$ provided that an intensity q is assigned to the lung nodule while the other current intensities in all its neighboring voxels over the characteristic neighborhoods $\mathbf{n}_\nu$; $\nu \in \mathbf{N}$, remains fixed:

$$E_{\mathbf{P}}(q|\mathbf{S}) = V_{\text{vx,nl}}(q) + \sum_{\nu\in\mathbf{N}}\sum_{(\xi,\eta,\gamma)\in\mathbf{n}_\nu}\left(V_{\nu,\text{nl}}(g_{x-\xi,y-\eta,z-\gamma},q) + V_{\nu,\text{nl}}(q,g_{x+\xi,y+\eta,z+\gamma})\right)$$

After the changes in the total energy, $E_{\mathbf{B}}$, of the 3D region $\mathbf{R_B} \subset \mathbf{R}$ inside the evolving boundary $\mathbf{B}$:

$$E_{\mathbf{B}} = \sum_{\forall\mathbf{P}=(x,y,z)\in\mathbf{R_B}} E_{\mathbf{P}}(g_{x,y,z}|\mathbf{S}) \tag{6}$$

stop, the evolution terminates.

2.2 Spherical Harmonics (SHs) Shape Analysis

Spectral SH analysis [1] considers 3D surface data as a linear combination of specific basis functions. In our case, the surface of the segmented lung nodule is approximated first by a triangulated 3D mesh (see Fig. 2) built with an algorithm by Fang and Boas [5]. Secondly, the lung nodule surface for each subject is mapped for the SH decomposition to the unit sphere. We propose a novel mapping approach, called "*Attraction-Repulsion*" that calls for all mesh nodes to meet two conditions: (*i*) the unit distance of each node from the lung nodule center as shown in Fig. 3, and (*ii*) an equal distance of each node from all of its nearest neighbors as shown in Fig. 4.

To detail our Attraction-Repulsion Algorithm (see its summary in Algorithm 1), let τ denote the iteration index, I be the total number of the mesh nodes (in all the experiments below $I = 4896$ nodes), and $\mathbf{P}_{\tau,i}$ be the Cartesian coordinates of the surface node i at iteration τ; $i = 1,\ldots,I$. Let J be the number of the neighbors for a mesh node (see e.g. Fig. 4) and $d_{\tau,ij}$ denote the Euclidean distance between the surface nodes i and j at iteration τ (as shown in Fig. 4(b)), where $i = 1,\ldots,I$ and $j = 1,\ldots,J$. Let $\mathbf{\Delta}_{\tau,ji} = \mathbf{P}_{\tau,j} - \mathbf{P}_{\tau,i}$ denote the displacement between the nodes j and i at iteration τ. Let $C_{\text{A},1}$, $C_{\text{A},2}$, C_{R} be the attraction and repulsion constants, respectively, that control the displacement of each surface node.

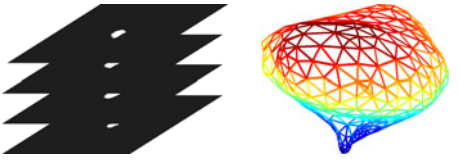

Fig. 2. Generating a 3D mesh for the lung nodule surface from a stack of successive segmented 2D LDCT slices

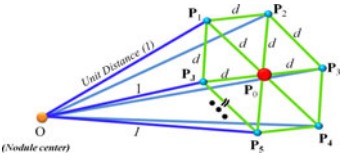

Fig. 3. 3D illustration of the unit distance from all surface nodes to the center of the lung nodule

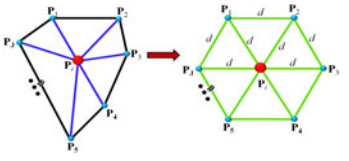

(a) (b)

Fig. 4. 2D illustration of the neighbors rearrangement: initial (a) vs. final equidistant locations (b) in all the directions.

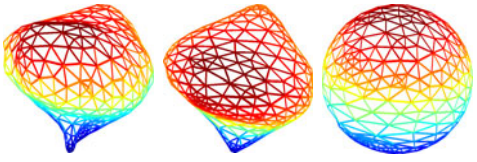

(a) (b) (c)

Fig. 5. Lung nodule mesh (a), its smoothed version (b), and the Attraction-Repulsion mapping to the unit sphere (c)

Algorithm 1: Attraction-Repulsion Algorithm

Initialization
- Construct the 3D lung nodule mesh (Fig. 5,a).
- Smooth it by the Laplacian filtering (Fig. 5,b).
- Initialize the mapping of the smoothed mesh to the unit sphere.

Repeat
- **For** $i = 1 \longrightarrow I$
  - **Attraction:**
    - Select a node to process.
    - Update the node using Eq. (7).
  - **Repulsion:**
    - Update the node using Eq. (8).
- **End** (all nodes in the mesh are shifted and back-projected onto the unit sphere).

While changes in the node positions occur (Fig. 5,c).

The starting attraction step of the proposed mapping tends to center each node $\mathbf{P}_i$; $i = 1, \ldots, I$, with respect to its neighbors by iteratively adjusting its location:

$$\mathbf{P}'_{\tau,i} = \mathbf{P}_{\tau,i} + C_{\mathrm{A},1} \sum_{j=1;j\neq i}^{J} \boldsymbol{\Delta}_{\tau,ji} d^2_{\tau,ji} + C_{\mathrm{A},2} \frac{\boldsymbol{\Delta}_{\tau,ji}}{d_{\tau,ji}} \tag{7}$$

where the factor $C_{\mathrm{A},2}$ keeps the tightly packed nodes from collision and also pushes the adjusted nodes away from their neighbors if a certain neighbor is much closer than the others.

The subsequent repulsion step inflates the whole mesh by pushing all the nodes outward to become evenly spaced after their final back-projection onto the unit sphere along the rays from the center of the sphere. To ensure that the nodes that have not been shifted will not collide with the altered node, the location of each node $\mathbf{P}_i$; $i = 1, \ldots, I$, is updated before the back-projection as follows:

$$\mathbf{P}^{\circ}_{\tau+1,i} = \mathbf{P}'_{\tau,i} + \frac{C_{\mathrm{R}}}{2I} \sum_{j=1;j\neq i}^{I} \left(\frac{\mathbf{\Delta}_{\tau,ji}}{|\mathbf{\Delta}_{\tau,ji}|^2} \right) \tag{8}$$

where a repulsion constant C_{R} controls the displacement of each surface node and establishes a balance between the processing time and accuracy (e.g. a smaller C_{R} values guarantees that the node faces will not become crossed during the iterations at the expense of the increased processing time). All the experiments below were obtained with $0.3 \leq C_{\mathrm{R}} \leq 0.7$.

The original lung nodule mapped to the unit sphere with the proposed Attraction-Repulsion algorithm is approximated by a linear combination of SHs, the lower-order harmonics being sufficient to represent more generic information, while the finer details requiring the higher - order ones. The SHs are generated by the solving an isotropic heat equation for the nodule surface on the unit sphere. Let $\mathcal{S} : \mathbf{M} \rightarrow \mathbf{U}$ denote the mapping of a nodule mesh $\mathbf{M}$ to the unit sphere $\mathbf{U}$. Each node $\mathbf{P} = (x, y, z) \in \mathbf{M}$ mapped to the spherical position $\mathbf{u} = S(\mathbf{P})$ is represented by the spherical coordinate $\mathbf{u} = (\sin\theta\cos\varphi, \sin\theta\sin\varphi, \cos\theta)$; where $\theta \in [0, \pi]$ and $\varphi \in [0, 2\pi)$ are the polar and azimuth angles, respectively. The SH $Y_{\alpha\beta}$ of degree α and order β is defined as [2]:

$$Y_{\alpha\beta} = \begin{cases} c_{\alpha\beta} G_{\alpha}^{|\beta|} \cos\theta \sin(|\beta|\varphi) & -\alpha \leq \beta \leq -1 \\ \frac{c_{\alpha\beta}}{\sqrt{2}} G_{\alpha}^{|\beta|} \cos\theta & \beta = 0 \\ c_{\alpha\beta} G_{\alpha}^{|\beta|} \cos\theta \cos(|\beta|\varphi) & 1 \leq \beta \leq \alpha \end{cases} \tag{9}$$

where $c_{\alpha\beta} = \left(\frac{2\alpha+1}{2\pi} \frac{(\alpha-|\beta|)!}{(\alpha+|\beta|)!} \right)^{\frac{1}{2}}$ and $G_{\alpha}^{|\beta|}$ is the associated Legendre polynomial of degree α and order β. For the fixed α, the polynomials G_{α}^{β} are orthogonal over the range $[-1, 1]$. As shown in [2], the Legendre polynomials are effective in calculating SHs, and this is the main motivation behind their use in this work.

Finally, the lung nodule is reconstructed from the SHs of Eq. (9). In the case of the SHs expansion, the standard least-square fitting does not accurately model the 3D shape of the lung nodule and can miss some of the shape details that discriminate between the malignant and benign lung nodules. To circumvent this problem, we used the iterative residual fitting by Shen and Chung [15] that accurately approximates the 3D shape of malignant and benign lung nodules. As demonstrated in Fig. 6, the model accuracy does not significantly change for the benign nodule from the 15 to 60 SHs, while it continues to increase for the malignant nodule.

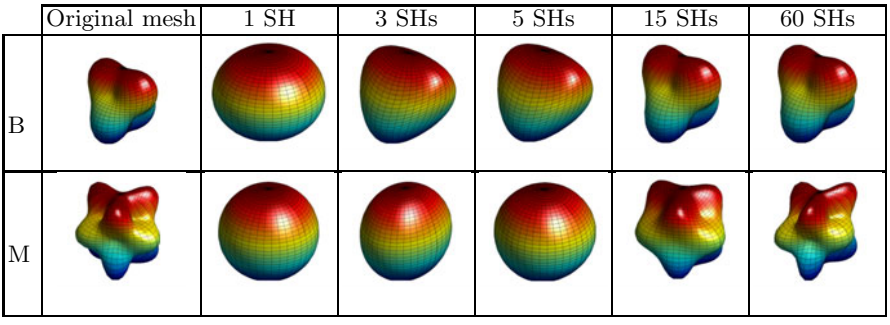

Fig. 6. 3D shape approximation for malignant (M) and benign (B) lung nodules

2.3 Quantitative Lung Nodule Shape Analysis

Our main hypothesis is that the shape of malignant nodules is more complicated (e.g., with spiculation) if it is compared with the shape of benign nodules which is simpler (smoothed shape) as shown in Fig. 6, so that more SHs have to be used for accurate approximation of the shape of the malignant lung nodule. Therefore, the number of the SHs after which there are no significant changes in the approximations can be used as a new shape index quantifying the shape complexity of the detected lung nodules. Due to the unit sphere mapping, the original mesh for each nodule is inherently aligned with the mesh for the approximate shape, and the sum of the Euclidean distances between the corresponding nodes gives the total error between both the mesh models. As shown in Fig. 7, the total error curves for the increasing number $\mathcal{K}$ of the SHs can be statistically analyzed to differentiate between the subjects.

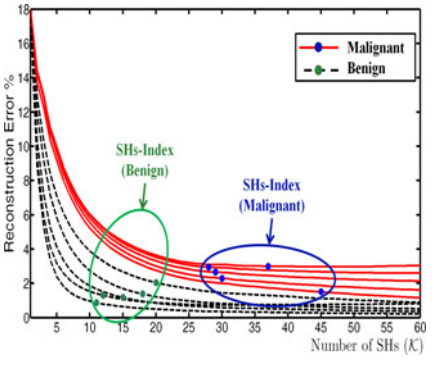

Fig. 7. Estimation of the shape index from the total nodule approximation error for malignant and benign nodules

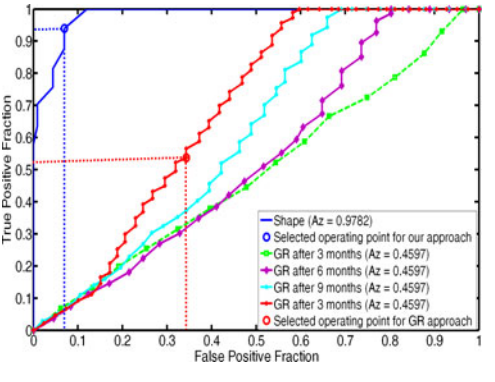

Fig. 8. The ROC curves for the proposed approach and the growth rate based diagnostic approach. Note that 'GR' stands for the growth rate.

3 Experimental Results and Conclusions

To justify the proposed methodology of analyzing the 3D shape of both malignant and benign nodules, the above proposed shape analysis framework was pilot-tested on a database of clinical multislice chest LDCT scans of 327 lung nodules (153 malignant and 174 benign). The CT data sets each have $0.7 \times 0.7 \times 2.0$ mm^3 voxels, with nodule diameters ranging from 3 mm to 30 mm. Note that these 327 nodules were diagnosed using a biopsy (our ground truth).

Segmentation results: Figure 9 illustrates results of segmenting pleural attached nodules shown by axial, sagittal, and coronal cross sections. The pixel-wise Gibbs energies in each cross section are higher for the nodules than for any other lung voxels including the attached artery. Therefore, our approach separates accurately the pulmonary nodules from any part of the attached artery. The evolution terminates after 50 iterations because the changes in the total energy become close to zero. The error of our segmentation with respect to the radiologist "ground truth" is 1.86%. In total, our segmentation of the 327 nodules has an error range of 0.29% – 2.17% with a mean error of 0.71%, and a standard error deviation of 1.21%.

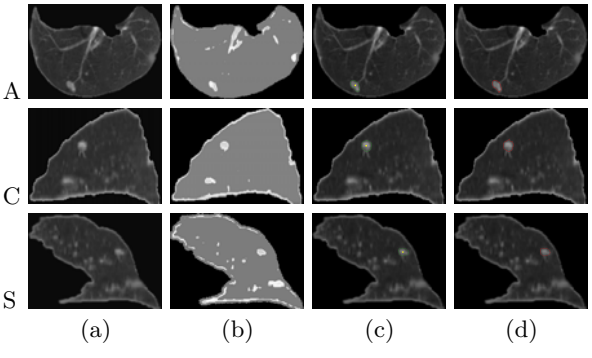

Fig. 9. 3D segmentation of pleural attached nodules; results are projected onto 2D axial (A), coronal (C), and saggital (S) planes for visualization: 2D profile of the original nodule (a), pixel-wise Gibbs energies (b) for $\nu \leq 11$, our segmentation (c), and (d) the radiologist's segmentation.

Diagnostic results: The training subset for classification (15 malignant lung nodules and 15 benign lung nodules) was arbitrarily selected among all of the 327 lung nodules. The accuracy of classification based on using K-nearest classifier of both the training and test subjects was evaluated using the χ^2-test at 95% confidence level. At the 95% confidence level, the correctly classified 143 out of 153 malignant nodules (a 93.5% accuracy), and 163 out of 174 control subjects (a 93.7% accuracy). The overall accuracy using the proposed 3D shape-based CAD system for 95% confidence level is 93.6% in **the first detection of lung nodules**. The classification based on traditional growth rate approach [14] **over**

one year is 87 out of 153 malignant nodules (a 56.9% accuracy), and 114 out of 174 benign nodules (a 65.7% accuracy) at a 95% confidence level, these results highlight the advantage of the proposed shape-based diagnostic approach.

Another way to measure and test the performance of the proposed diagnostic system is to compute the receiver operating characteristic (ROC). Each point on the graph is generated by using a different cut point (classification threshold). Figure 8 shows the ROC of the two approaches; our proposed shape index based diagnostic approach and the growth rate based diagnostic approach [14]. It is clear from Fig 8 that the area under ROC curve of our present approach is larger (Az = 0.9782) than the area under the ROC curve of the growth rate-based diagnostic approach [14] (Az is 0.6757 for one year estimated growth rate). The high sensitivity and specificity of the proposed approach is due to using the estimated number of spherical harmonic to approximate the 3D shape of the detected lung nodule as a new discriminatory feature which is more separable than using the estimated growth rate.

As demonstrated in this paper, the preliminary results justify further elaboration of the proposed alternative method for diagnosing malignant lung nodules. Its novelty lies in using the shape of a segmented 3D nodule instead of the more conventional growth rate as a reliable diagnostic feature. The shape is described in terms of a linear combination of spherical harmonics (SHs).

The proposed nodule shape analysis could lead to more accurate, faster, and more clinically useful diagnostics of detected pulmonary nodules without the need for investigating their temporal development on the successive LDCT images of the same subject collected for a relatively long time. The present C++ implementation on the Intel quad processor (3.2GHz each) with 16 GB memory and 1.5 TB hard drive with the RAID technology takes approximately 7 sec for processing 30 mm lung nodules and less than 3 sec for processing 5 mm lung nodules.

References

1. Chung, M.K., Shen, L., Dalton, K.M., Evans, A.C., Davidson, R.J.: Weighted fourier series representation and its application to quantifying the amount of gray matter. IEEE Trans. Med. Imag. 26, 566–581 (2007)
2. Courant, R., Hilbert, D.: Methods of Mathematical Physics, vol. II. Interscience, New York (1953)
3. El-Baz, A., Gimel'farb, G.: Em based approximation of empirical distributions with linear combinations of discrete gaussians. In: Proc. IEEE Int. Conf. Image Process (ICIP 2007), San Antonio, Texas, USA, September 16-19, vol. IV, pp. 373–376 (2007)
4. El-Ba, A., Gimel'farb, G.G., Falk, R., Holland, T., Shaffer, T.: A new stochastic framework for accurate lung segmentation. In: Metaxas, D., Axel, L., Fichtinger, G., Székely, G. (eds.) MICCAI 2008, Part I. LNCS, vol. 5241, pp. 322–330. Springer, Heidelberg (2008)
5. Fang, Q., Boas, D.: Tetrahedral mesh generation from volumetric binary and grayscale images. In: Proc. IEEE Int. Symp. on Biomed. Imag. From Nano to Macro (ISBI 2009), Boston, MA, USA, June 28-July 1, pp. 1142–1145 (2009)

6. Farag, A.A., El-Baz, A.S., Gimel'farb, G.G., Falk, R., El-Ghar, M.A., Eldiasty, T., Elshazly, S.: Appearance models for robust segmentation of pulmonary nodules in 3D LDCT chest images. In: Larsen, R., Nielsen, M., Sporring, J. (eds.) MICCAI 2006. LNCS, vol. 4190, pp. 662–670. Springer, Heidelberg (2006)
7. Furuya, K., Murayama, S., Soeda, H., Murakami, J., Ichinose, Y., Yabuuchi, H., Katsuda, Y., Koga, M., Masuda, K.: New classification of small pulmonary nodules by margin characteristics on high-resolution ct. Acta Radiologica 40, 496–504 (1999)
8. Gurney, W., Swensen, S.: Solitary pulmonary nodules: determining the likelihood of malignancy with neural network analysiss. Radiology 196, 823–829 (1995)
9. Kass, M., Witkin, A., Terzopoulos, D.: Snakes: Active contour models. Int. J. Computer Vision 1, 321–331 (1987)
10. Kawata, Y., Niki, N., Ohmatsu, H., Kakinuma, R., Eguchi, K., Kaneko, M., Moriyama, N.: Biexponential characterization of prostate tissue water diffusion decay curves over an extended b-factor range. IEEE Trans. Nucl. Sci. 45, 2132–2138 (1998)
11. Kawata, Y., Niki, N., Ohmatsu, H., Kusumoto, M., Kakinuma, R., Mori, K., Nishiyama, H., Eguchi, K., Kaneko, M., Moriyama, N.: Computerized analysis of 3-d pulmonary nodule images in surrounding and internal structure feature spaces. In: Proc. Int. Conf. Image Process., pp. 889–892 (2001)
12. Kido, S., Kuriyama, K., Higashiyama, M., Kasugai, T., Kuroda, C.: Fractal analysis of small peripheral pulmonary nodules in thin-section ct: evaluation of the lung-nodule interfaces. J. Comput. Assist. Tomogr. 26, 573–578 (2002)
13. Mori, K., Niki, N., Kondo, T., Kamiyama, Y., Kodama, T., Kawada, Y., Moriyama, N.: Development of a novel computer-aided diagnosis system for automatic discrimination of malignant from benign solitary pulmonary nodules on thin-section dynamic computed tomography. J. Comput. Assist. Tomogr. 29, 215–222 (2005)
14. Reeves, A., Chan, A., Yankelevitz, D., Henschke, C., Kressler, B., Kostis, W.: On measuring the change in size of pulmonary nodules. IEEE Trans. Med. Imag. 25, 435–449 (2006)
15. Shen, L., Chung, M.K.: Large-scale modeling of parametric surfaces using spherical harmonics. In: Proc. 3rd Int. Symp. 3D Data Process. Visualiz. Transmission, Chapel Hill, NC, USA, June 14-16, pp. 294–301 (2006)
16. Weir, H.K., Thun, M.J., Hankey, B.F., Ries, L.A., Howe, H.L., Wingo, P.A., Jemal, A., Ward, E., Anderson, R.N., Edwards, B.K.: Annual report to the nation on the status of cancer, 1975-2000. J. National Cancer Institute 95, 1276–1299 (2003)